Structural insights into the enzyme specificity of a novel ω-transaminase from the thermophilic bacterium *Sphaerobacter thermophilus*

Sunghark Kwon[a], Jun Hyuck Lee[b], Chang Min Kim[a], Hyun Ji Ha[a], Sung Hoon Lee[a], Chang Sup Lee[c], Ju-Hong Jeon[d], Insuk So[d], Hyun Ho Park[a,*]

[a] *College of Pharmacy, Chung-Ang University, Seoul 06974, Republic of Korea*
[b] *Unit of Research for Practical Application, Korea Polar Research Institute, Incheon 21990, Republic of Korea*
[c] *College of Pharmacy and Research Institute of Pharmaceutical Science, Gyeongsang National University, Jinju 52828, Republic of Korea*
[d] *Department of Physiology and Biomedical Sciences, Institute of Human-Environment Interface Biology, Seoul National University College of Medicine, Seoul 03080, Republic of Korea*

ARTICLE INFO

ABSTRACT

Transaminases are pyridoxal 5′-phosphate-dependent enzymes that reversibly catalyze transamination reactions from an amino group donor substrate to an amino group acceptor substrate. ω-Transaminases (ωTAs) utilize compounds with an amino group not at α-carbon position as their amino group donor substrates. Recently, a novel ωTA with broad substrate specificity and high thermostability from the thermophilic bacterium *Sphaerobacter thermophilus* (St-ωTA) has been reported. Although St-ωTA has been biochemically characterized, little is known about its determinants of substrate specificity. In the present study, we determined the crystal structure of St-ωTA at 1.9 Å resolution to clarify in detail its mechanism of substrate recognition. The structure of St-ωTA revealed that it has a voluminous active site resulting from the unique spatial arrangement of residues comprising its active site. In addition, our molecular docking simulation results suggest that substrate compounds may bind to active site residues via electrostatic interactions or hydrophobic interactions that can be induced by subtle rearrangements of active site residues. On the basis of these structural analyses, we propose a plausible working model of the enzymatic mechanism of St-ωTA. Our results provide profound structural insights into the substrate specificity of St-ωTA and extend the boundaries of knowledge of TAs.

1. Introduction

Transaminases catalyze reversible transamination reactions by acting on an amino group donor and an amino group acceptor (Cooper and Meister, 1989). The amino group transfer is mediated by a pyridoxal 5′-phosphate (PLP) molecule positioned in the active site (Hayashi, 1995; Toney, 2011). In general, transaminases recognizing an amino group bound to any carbon position other than α-carbon are categorized as ω-transaminases (ωTAs) (Malik et al., 2012; Bezsudnova et al., 2017). ωTAs also recognize some ketone compounds, such as pyruvate and α-ketoglutarate, as amino group acceptors (Malik et al., 2012; Bezsudnova et al., 2017). To date, ωTAs have gained much attention owing to their high utility values in the fields of fine chemistry and pharmaceutics (Fuchs et al., 2015; Guo and Berglund, 2017; Slabu et al., 2017). Specifically, ωTAs are potential biocatalysts for asymmetric synthesis and kinetic resolution of racemic compounds because they have (*S*)- or (*R*)-enantioselectivity for their amino group donor

substrates (Fuchs et al., 2015; Koszelewski et al., 2010a,b).

A gene encoding an ωTA from the thermophilic bacterium *Sphaerobacter thermophilus* (St-ωTA) was identified based on homology to sequence for an ωTA from the mesophilic bacterium *Polaromonas* sp. JS666 as published in a previous study (Mathew et al., 2016). It has also been demonstrated that St-ωTA possesses catalytic activity toward various substrates including both β- and γ-amino acids as amino group donor substrates (Mathew et al., 2016). This exceptional property of St-ωTA may significantly expand substrate diversity applicable to kinetic resolution of racemic compounds. Moreover, St-ωTA has been shown to exhibit thermostability, maintaining catalytic activity up to 60 °C under experimental conditions (Mathew et al., 2016), which indicates that it is suitable for use as an industrial biocatalyst under harsh conditions such as high temperature. Another notable feature of St-ωTA is that it prefers aromatic amino acids to aliphatic ones as amino group donors regardless of the carbon position of the amino group (Mathew et al., 2016). Given that a number of active pharmaceutical ingredients and

their precursors are aromatic compounds, such an enzymatic property allows us to utilize St-ωTA as a specialized tool for production of valuable pharmaceutical compounds.

Prior research on St-ωTA has focused mainly on substrate screening and enzymatic optimization *in vitro* (Mathew et al., 2016). In addition, relatively little attention has been paid to the enzymatic ability to use ketone compounds as amino group acceptors, compared with its ability to use amines and amino acids as amino group donors. Previous research also fails to address how St-ωTA can recognize diverse substrates, and its preference for aromatic compounds remains unclear. Addressing these issues will require structural information on St-ωTA. Therefore, it is necessary to determine the structure of St-ωTA and explain its substrate recognition mechanism based on this structural information.

In the present study, we report the crystal structure of St-ωTA at 1.9 Å resolution, and use this solved structure to perform molecular docking simulations with diverse candidate substrates to elucidate the specific substrate recognition mechanism of St-ωTA. Our structural analyses, together with molecular docking simulations, show how St-ωTA can recognize a wide range of amino group donor and acceptor substrates. Accordingly, the results presented in this paper provide valuable structural information for ωTA engineering to improve its enzymatic activity and produce useful compounds.

2. Materials and methods

2.1. Overexpression and purification

The expression vector for St-ωTA was constructed as described previously (Mathew et al., 2016). *Escherichia coli* strain BL21(DE3) cells were transformed with this vector and plated on lysogeny broth (LB) agar containing 50 μg/mL kanamycin. A well-formed colony was selected and cultured overnight in 5 mL LB medium containing 50 μg/mL kanamycin with shaking at 37 °C. This cell suspension was transferred into 1 L LB medium for large scale culture. When the optical density value at 600 nm reached approximately 0.7, 0.5 mM isopropyl β-D-1-thiogalactopyranoside was added to induce overexpression. Cells were further cultured by agitating at 20 °C for 18 h. Cells were then harvested by centrifugation at 35,000 rpm for 15 min, flash-frozen with liquid N_2, and stored at −80 °C until use.

Frozen cells were thawed and resuspended in buffer A [20 mM Tris-HCl (pH 7.9), 500 mM NaCl, and 25 mM imidazole] supplemented with phenylmethanesulfonyl fluoride (Sigma-Aldrich) as a protease inhibitor. Cells were disrupted by sonication on ice with six repeated 30 s bursts and 1 min intervals between each burst. Cell debris was removed by centrifugation at 16,000 rpm for 30 min at 4 °C. The supernatant was mixed with Ni-nitrilotriacetic acid agarose (Qiagen) and gently agitated at 4 °C overnight. The mixture was then loaded onto a gravity-flow column pre-equilibrated with buffer A. The packed column was washed with buffer B [20 mM Tris-HCl (pH 8.0), 500 mM NaCl, and 60 mM imidazole]. Subsequently, the bound protein was eluted with buffer C [20 mM Tris-HCl (pH 8.0), 500 mM NaCl, and 250 mM imidazole]. The eluate was subjected to size exclusion chromatography (SEC) for further purification. The sample was loaded onto a Superdex 200 10/300 GL 24 mL column (GE Healthcare) pre-equilibrated with buffer D [20 mM Tris-HCl (pH 8.0), 150 mM NaCl]. SEC purification was carried out using an ÄKTA explorer system (GE Healthcare). Purified protein was concentrated to 6.2 mg/mL using a Vivaspin centrifugal filter (Sartorius), flash-frozen in liquid N_2, and stored at −80 °C until use. Protein purity at each purification step was assessed by sodium dodecyl sulfate-polyacrylamide gel electrophoresis.

2.2. Crystallization and data collection

Crystallization conditions were initially screened using the hanging drop vapor diffusion method and several commercial crystallization kits including Wizard I and II (Hampton Research). One microliter of protein solution was mixed with an equal volume of reservoir solution, and the droplet was equilibrated with 300 μL of the mother liquor at 20 °C. Crystals were obtained from a crystallization buffer composed of 0.1 M sodium acetate (pH 4.5), 1.2 M K_2HPO_4, and 0.8 M NaH_2PO_4. This crystallization condition was finally optimized to 0.1 M sodium acetate (pH 4.8), 1.2 M K_2HPO_4, 0.9 M NaH_2PO_4, and 40% (v/v) 2,5-hexanediol. Crystals with diffraction quality appeared in 3 days. The crystals were soaked in a cryoprotectant solution consisting of the reservoir solution supplemented with 48% (v/v) glycerol. Crystals were mounted and flash-cooled in an N_2 stream at −178 °C. X-ray diffraction data were collected on the Pohang Accelerator Laboratory (PAL; Pohang, Korea) 5C beamline. The diffraction data were indexed, integrated, and scaled with HKL2000 (Otwinowski and Minor, 1997).

2.3. Structure determination and refinement

The crystal structure was determined by the molecular replacement method using Phaser (McCoy et al., 2007) embedded in the CCP4 program package suite (Winn et al., 2011). The structure of a β-phenylalanine aminotransferase from *Variovorax paradoxus* (PDB ID: 4AO9; 39% sequence identity) (Crismaru et al., 2013) was used as a search model. The initial model was built with Coot (Emsley and Cowtan, 2004) and refined using Refmac5 (Murshudov et al., 2011) and phenix.refine (Afonine et al., 2012) in Phenix (Adams et al., 2010), respectively. Water molecules were added automatically with ARP/wARP (Langer et al., 2008). The quality of the final model was found to be reasonable using Procheck (Laskowski et al., 1993). The data collection and refinement statistics are summarized in Table 1. All structural figures were generated using Pymol (Schrödinger, 2006), LigPlot+ (Laskowski and Swindells, 2011), and AutoDockTools 1.5.6. (Morris et al., 2009) Multiple sequence alignment was conducted and displayed using Clustal Omega (Sievers et al., 2011) and ESPript 3.0 (Robert and

Table 1
Data collection and refinement statistics for St-ωTA.

Data collection	
Space group	$P2_12_12_1$
Unit cell parameter *a, b, c* (Å)	
a, b, c (Å)	a = 82.06, b = 61.25, c = 185.39
α, β, γ (°)	α = β = γ = 90
Resolution range (Å)[1]	50.00–1.90 (1.93–1.90)
Total reflections	412,504
Unique reflections	63,258
Multiplicity	6.5 (6.3)
Completeness (%)[1]	85.2 (82.8)
Mean $I/\sigma(I)$[1]	26.1 (4.4)
R_{merge} (%)[1,2]	11.4 (62.1)
$CC_{1/2}$ (%)[1]	95.6 (81.2)
Wilson *B*-factor (Å²)	14.3
Refinement	
Resolution range (Å)	29.85–1.90
Reflections	61,941
Reflections (test set)	3133
R_{work} (%)	15.6
R_{free} (%)	19.4
No. of molecules in the asymmetric unit	2
No. of protein atoms/water molecules	6605/1031
Average *B*-factor values of protein/water (Å²)	14.3/25.4
Ramachandran plot[3]:	
favored/outliers (%)	98.2/0.0
Rotamer outliers (%)	0.0
RMSD bonds (Å)/angles (°)	0.007/0.94

[1] Values for the outermost resolution shell in parentheses.
[2] $R_{merge} = \Sigma_h \Sigma_i |I(h)_i - <I(h)>|/\Sigma_h \Sigma_i I(h)_i$, where $I(h)$ is the observed intensity of reflection h, and $<I(h)>$ is the average intensity obtained from multiple measurements.
[3] Calculated by Procheck.

Gouet, 2014), respectively.

2.4. Molecular docking simulations

Models of candidate substrate structures for St-ωTA were built using Avogadro (Hanwell et al., 2012). The geometries of all structures were optimized to minimized energy values. The respective pdbqt files of St-ωTA and substrate compounds were generated using AutoDockTools 1.5.6. Key residues within the active site of St-ωTA were designated as flexible residues for accurate docking simulations. Values for the size and spacing of a grid box including the flexible residues were set to 20 Å × 20 Å × 20 Å and 1 Å, respectively. Other calculation parameters were assigned default values. Molecular docking simulations were carried out using Autodock Vina (Trott and Olson, 2010). A total of 15 different conformers per compound were generated after respective docking simulations. The resulting conformers were ranked using an energy scoring function.

2.5. Multiangle light scattering analysis

To measure the absolute molecular weight of St-ωTA in solution, SEC-coupled multi-angle light scattering (SEC-MALS) analysis was carried out using an ÄKTA explorer system. A protein solution sample was loaded onto a Superdex 200 10/300 GL 24 mL column pre-equilibrated with a buffer consisting of 20 mM Tris-HCl (pH 8.0) and 500 mM NaCl. The mobile phase solution was pumped at a flow rate of 0.4 mL/min at room temperature. A DAWN-treos MALS detector (Wyatt Technology) was used to detect scattered light. The molecular weight of bovine serum albumin was measured for a reference. Data were assessed using ASTRA software (Wyatt Technology).

2.6. UV–Visible spectroscopic analysis

A UV–Visible absorption spectroscopic analysis for St-ωTA was conducted using NanoPhotometer NP80 spectrophotometry (IMPEL) to confirm the covalent bond state of the cofactor in St-ωTA. A xenon flash lamp with a bandwidth of 1.8 nm was used as a light source. An absorption spectrum was obtained over a wavelength range of 200–900 nm. Wavelengths corresponding to each peak were analyzed to identify the respective molecules.

3. Results

3.1. Overall structure of St-ωTA

The structure of St-ωTA was determined at 1.9 Å resolution using the molecular replacement method. The values for R_{work} and R_{free} of the final model are 15.6% and 19.4%, respectively. The crystal structure of St-ωTA contains two monomers (subunit A and B) in the asymmetric unit (Fig. 1A). The two monomers form a dimer with non-crystallographic 2-fold symmetry. Our SEC-MALS analysis also indicates that the crystallographic dimeric state of St-ωTA is in accordance with a multimeric state in solution. The SEC-MALS analysis showed that a peak appeared at 20 mL retention volume with an absolute molecular weight of 99.9 kDa, which closely coincides with the theoretical molecular weight of St-ωTA containing a C-terminal His₆-tag (97.3 kDa) (Fig. 1B). Biophysical analysis using the PDBePISA server (Krissinel and Henrick, 2007) revealed that overall surface and buried areas in the dimeric form are 28,156 Å² and 10,452 Å², respectively. Thus, St-ωTA has a buried area of 5226 Å² per monomer, which means that 27% of the overall surface area of the monomer is buried at the interface upon the dimer formation. This interface region exhibited mostly high evolutionary conservation (Fig. 1C, D), based on analyses of the sequences of 150 proteins homologous to St-ωTA using the ConSurf server (Ashkenazy et al., 2010), which provides tools for the identification of evolutionary conservation in proteins. The interface score calculated by

the PDBePISA server was 0.923, implying that interactions at the interface are strong enough to maintain the dimeric form in solution. It has been reported that most ωTAs except for rare cases have a dimeric form in both crystal environment and solution, suggesting that the dimer is a multimeric state for its biological function (Hirotsu et al., 2005; Bezsudnova et al., 2017; Kwon and Park, 2019a). Thus, the dimeric state shown in St-ωTA is also assumed to constitute the biological functional unit in cellular environments.

The St-ωTA monomer consists of fourteen α-helices, eight 3₁₀-helices, and fourteen β-strands, with the typical fold adopted by other ωTAs (Fig. 1E). A structural analysis using the Dali server (Holm and Laakso, 2016) showed that the St-ωTA structure shares its overall architecture with the β-phenylalanine aminotransferase from *Variovorax paradoxus* (Z-score = 48.3; root-mean-square deviation (RMSD) = 1.7 Å; sequence identity = 39%; PDB ID: 4AO9) (Crismaru et al., 2013) used to determine the phase of St-ωTA, but exhibits the highest similarity to the structure of glutamate-1-semialdehyde 2,1-aminomutase from *Bacillus anthracis* (Z-score = 51.9; RMSD = 1.4 Å; sequence identity = 37%; PDB ID: 3K28). Each monomer of St-ωTA contains a PLP cofactor in the active site. Structural superimposition analysis revealed that the two molecules are almost identical to each other, exhibiting an RMSD value of 0.2 Å for 432 Cα atoms (Fig. S1). The monomer structure also comprises a large domain (T101-P309) and a small domain, which is composed of the N-terminal lobe (M1-P100) and the C-terminal lobe (P310-G446) (Fig. 1E). It is noteworthy that the small domain is divided into two distinct segments of amino acid sequence, but constitutes a spatial continuum. This domain composition is a common structural feature observed in ωTAs.

3.2. Active site structure of St-ωTA

To infer the active site residues of St-ωTA, we aligned the sequence with those of a β-TA from *Variovorax paradoxus* (Vp-βTA; sequence identity = 39%) (Crismaru et al., 2013) and a β-TA from *Mesorhizobium* sp. strain LUK (Ms-βTA; sequence identity = 38%) (Wybenga et al., 2012), in which residues comprising the active site have been proposed, or are known, respectively (Fig. S2). On the basis of this multiple sequence alignment, we predict that Arg36, Thr38, Tyr71, Tyr154, Arg226, Ser227, Ala416, and Phe418, together with Gly315 from the other subunit contribute to formation of the active site (Fig. 2A). These residues are located near the PLP cofactor, which is positioned at the bottom of the active site. As in other TAs, the putative active site of St-ωTA is located in proximity to the interface of the two subunits (Fig. 2B). In addition, the distance from the surface to the PLP molecule within a deep funnel-like cavity is approximately 30 Å.

It is well known that TAs have two pockets at their active site, one of which is positioned near the phosphate group of PLP, and the other is located in the vicinity of the oxygen atom on the PLP ring (Oosterwijk et al., 2016; Bezsudnova et al., 2017; Slabu et al., 2017). The fact that the size of the two pockets depends on the species from which a TA originates is another intriguing feature of TAs (Schiroli and Peracchi, 2015; Slabu et al., 2017). We found that St-ωTA also has two distinct, different sized pockets in its active site (Fig. 2C, D). Specifically, the O-pocket (large pocket) comprises Thr38, Tyr71, Tyr154, Arg226, Ser227, Ala416, and Phe418, together with Gly315 from the other subunit (Fig. 2C), whereas P-pocket (small pocket) formation is associated with Arg36 (Fig. 2D). Given that a hydrophilic residue such as Arg36 forms the P-pocket, and many hydrophobic residues participate in forming the O-pocket, it is reasonable to assume that the hydrophilic moiety of the substrate faces the P-pocket, while the hydrophobic group occupies the O-pocket.

The PLP cofactor in each subunit is covalently linked to the adjacent Lys282 residue, forming lysine-pyridoxal-5′-phosphate (LLP). Lys282 is considered to be a key residue for the catalytic reaction (Fig. 2A). The omit maps of PLP and Lys282 clearly show a covalent bond between the two molecules in both subunit A and B (Fig. S3). The PLP molecule
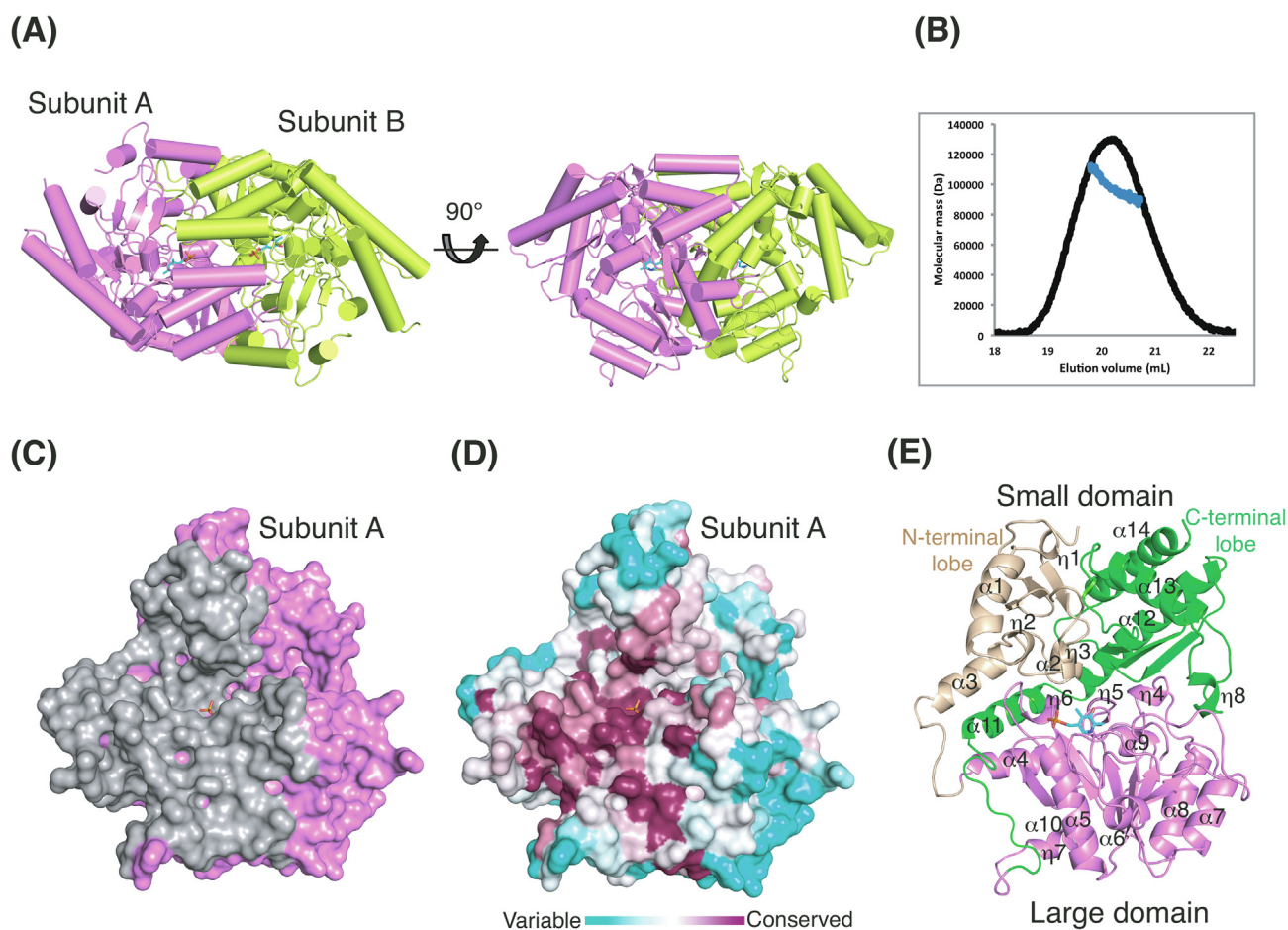
Fig. 1. Structure of St-ωTA. (A) Overall structure of St-ωTA. The dimeric structure is represented in two different perspectives in cartoon rendering. Subunits A and B are colored violet and limon, respectively. The PLP molecule in each subunit is depicted as sticks. (B) SEC-MALS profile of St-ωTA. SEC-coupled MALS data (blue) are plotted as elution volume (x-axis) and molecular mass (y-axis) distributions and superimposed on the SEC chromatogram (black) at 280 nm. (C) A sectional view of subunit A. PLP and the interface are represented as sticks and grey surface, respectively. (D) Surface representation of subunit A colored by the degree of sequence conservation. The perspective is the same as that in panel C. (E) The monomer structure of St-ωTA comprising a large domain (residues 101–309; violet) and a small domain (residues 1–100 and 310–449). The small domain is subdivided into two pieces (N- and C-terminal lobes): N-terminal lobe (residues 1–100; wheat) and C-terminal lobe (residues 310–449; green).

interacts with the proximal residues and with several water molecules (Fig. 2E). Specifically, the nitrogen and oxygen atoms on the PLP ring form hydrogen bonds to Asp255, and to a water molecule bound to Arg266, respectively. The phosphate group of PLP also forms hydrogen bonds to Gly127, Thr128, and Thr317 in addition to some water-mediated interactions. Twelve water molecules are located in the vicinity of PLP and play a vital role in coordinating PLP-enzyme interactions. In addition to the hydrogen bonds, hydrophobic interactions with Val257, ILe258, and Gly316 are involved in PLP fixation.

Prior studies have demonstrated that the amino group of a donor substrate displaces the nitrogen atom of a Lys residue covalently bound to PLP, thereby converting PLP into pyridoxamine-5′-phosphate (PMP). The amino group of PMP is then sequentially transferred to an acceptor substrate (Park et al., 2012; Toney, 2011). In our crystal structure, the PLP molecule forms a covalent bond with Lys282, forming LLP (Fig. S3). This state (internal aldimine) corresponds to the "resting" state prior to the initiation step of the overall catalytic reaction cycle (Bezsudnova et al., 2017; Toney, 2011). In support of the electron density map, UV–Visible spectrometric analysis of St-ωTA confirmed the chemical state of the PLP molecule (Fig. 2F). Previous studies have shown that PLP bound to a Lys residue has an absorption peak at approximately 410–430 nm, while the absorption peak of the PMP form (Michaelis complex) appears at approximately 320–330 nm (Boyko et al., 2016). St-ωTA exhibited a distinct absorption peak at

approximately 420 nm (Fig. 2F). Accordingly, our crystal structure constitutes a snapshot of the structural geometry of St-ωTA prior to amino group transfer from a donor substrate.

3.3. Surface electrostatic properties of St-ωTA

To investigate the surface charge distribution of St-ωTA, electrostatic potential analysis was carried out using the Adaptive Poisson-Boltzmann Solver (Jurrus et al., 2018). This analysis revealed that the active site cavity consists of positively charged residues, while negatively charged residues are locally distributed in adjacent regions of the active site (Fig. 3A). Meanwhile, regions peripheral to the active site entrance display hydrophobicity on solvent accessible surfaces (Fig. 3B). In addition, we generated an electrostatic potential iso-contour map of St-ωTA (Fig. 3C). According to this map, two positively charged regions form the center of each active site, and a vast doughnut-shaped cloud of negative charges distributes around the active sites. A buffer zone exists between the two distinctly charged regions, which exhibits considerably weaker electrostatic charges. The weakened electrostatic properties of this zone are reasonable, given that this area corresponds to the hydrophobic region surrounding the active site entrance. These unique charge distributions can generate a strong electric field (Fig. 3D), implying that St-ωTA may exploit its electric field to attract a cofactor and substrates to its active site.
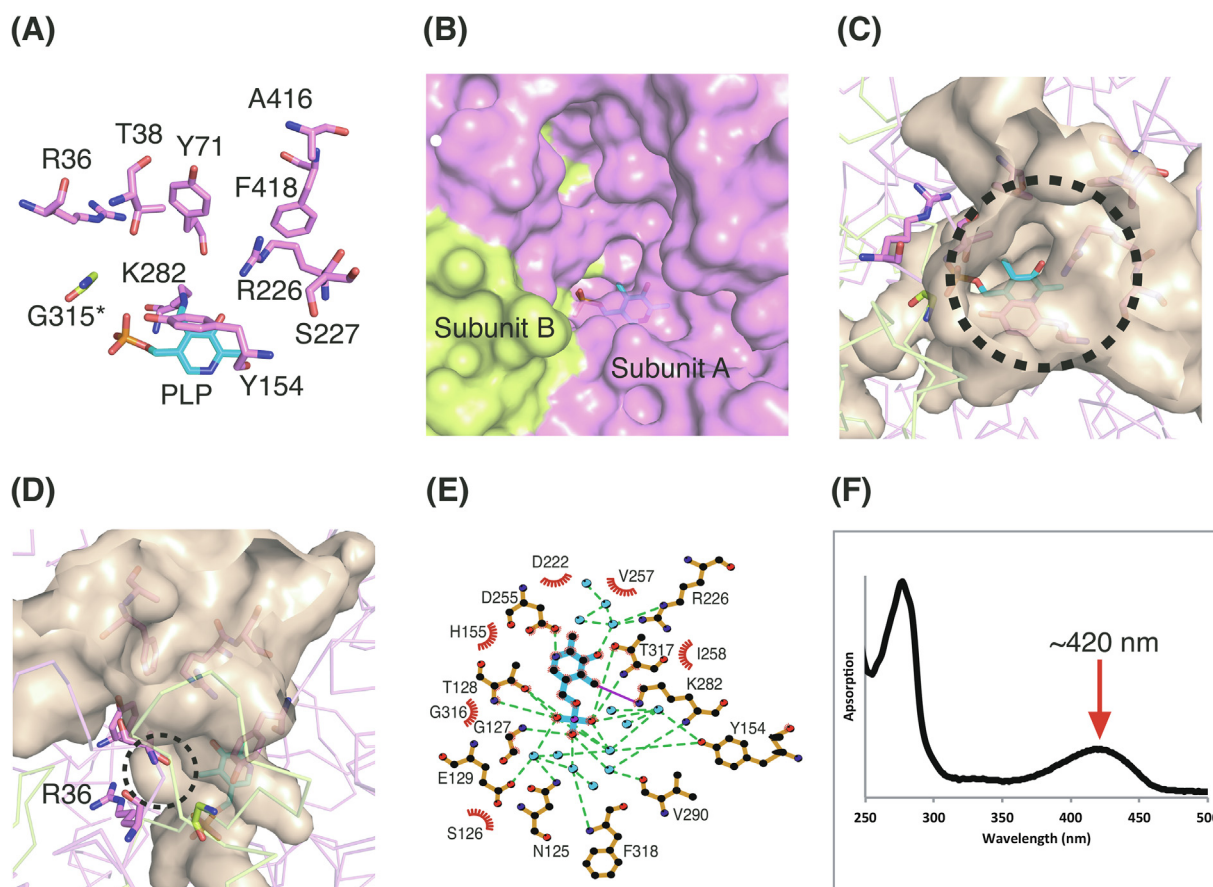
Fig. 2. Active site of St-ωTA. (A) Active site residues of subunit A. Gly315 from subunit B constitutes a component of the active site of subunit A. The asterisk by the G315 residue denotes that it emanates from the other subunit. (B) Active site cavity of St-ωTA. The PLP molecule is positioned in proximity to the interface of the two subunits. The O-pocket (C) and P-pocket (D) of the active site. Active site residues and PLP are represented as sticks. Dashed circles indicate the space occupied by the two pockets. (E) Diagram of PLP interactions with adjacent molecules in the active site. Blue circles and green dashed lines represent water molecules and hydrogen bonds, respectively. (F) UV–Visible spectrum of St-ωTA in solution. The red arrow indicates the absorption peak at approximately 420 nm.

3.4. Structural comparison with homologues

To identify structural features specific to St-ωTA, we compared the structure of St-ωTA with those of its homologues. Homologous proteins selected on the basis of sequence identity and tertiary structure similarity are as follows: a β-phenylalanine aminotransferase from *Variovorax paradoxus* (Vp-βTA; sequence identity = 39%; Z-score = 48.3; RMSD = 1.7 Å; PDB ID: 4AO9) (Crismaru et al., 2013), a β-aminotransferase from *Mesorhizobium* sp. LUK (Ms-βTA; sequence identity = 38%; Z-score = 48.1; RMSD = 1.8 Å; PDB ID: 2YKU) (Wybenga et al., 2012), a glutamate-1-semialdehyde 2,1-aminomutase from *Bacillus anthracis* (Ba-GSAM; sequence identity = 37%; Z-score = 51.9; RMSD = 1.4 Å; PDB ID: 3K28), a glutamate-1-semi-aldehyde 2,1-aminomutase from *Bacillus subtilis* (Bs-GSAM; sequence identity = 36%; Z-score = 49.3; RMSD = 1.8 Å; PDB ID: 3BS8) (Ge et al., 2010), a glutamate-1-semialdehyde 2,1-aminomutase from *Thermosynechococcus elongatus* (Te-GSAM; sequence identity = 37%; Z-score = 47.3; RMSD = 1.5 Å; PDB ID: 2CFB) (Schulze et al., 2006), and a glutamate-1-semialdehyde 2,1-aminomutase from *Aeropyrum pernix* (Ap-GSAM; sequence identity = 36%; Z-score = 49.2; RMSD = 1.7 Å; PDB ID: 2EPJ). The first four proteins are mesophilic enzymes, and the latter two are, in order, thermophilic and hyperthermophilc enzymes.

The structure of St-ωTA was initially compared with the structures of the four homologous enzymes from mesophiles. Comparative analysis revealed that the five enzymes are structurally similar to each other, exhibiting a common architecture (RMSD = 1.8–2.2 Å; Fig. 4A). Structural comparison of the active sites of St-ωTA, Vp-βTA, and Ms-βTA revealed similarities and differences in the spatial arrangement of

key residues (Fig. 4B). Although they share the structural properties of a small hydrophilic P-pocket and a large hydrophobic O-pocket, the length and spatial assignment of some residues exhibited remarkable differences. Specifically, while Vp-βTA and Ms-βTA have Val43 and Ile56 in the O-pocket, respectively, St-ωTA has Thr38 at the same position, suggesting that Thr38 may enable formation of a hydrogen bond with the substrate at the interface between the P- and O-pockets. Another notable difference is the identity of a residue which contributes to active site formation from the other subunit. In the cases of Vp-βTA and Ms-βTA, Ser298 and Ala312 are associated with O-pocket formation, respectively. In St-ωTA, however, Gly315 occupies the corresponding position, thereby somewhat expanding the O-pocket and moderating the hydrophilicity or hydrophobicity shown in the other enzymes. Most interestingly, we found that the spatial arrangements of Arg226 and Ala416 in St-ωTA are spatially inverted, compared with those of Vp-βTA and Ms-βTA (Fig. 4B). Arg226 and Ala416 of St-ωTA are located at the coordinates of Ala212 and Arg398 of Vp-βTA, respectively, which correspond to Ala225 and Arg412 of Ms-βTA. Moreover, the position of Ala416 of St-ωTA deviates from those of the respective Arg residues of Vp-βTA and Ms-βTA, thereby markedly enlarging the O-pocket. This distinctive space allocation within the O-pocket is assumed to constitute a key steric determinant of the unique substrate specificity of St-ωTA.

Based on our findings of different active site residue arrangements among these three TAs, we also analyzed their volumetric traits using the POCASA server (Yu et al., 2010), *au fond*, a server for predicting ligand-binding sites. The respective active site cavities, from their entrance to their bound PLP were defined using virtual probe spheres with a radius of 2 Å, to generate corresponding grid maps. Volumetric
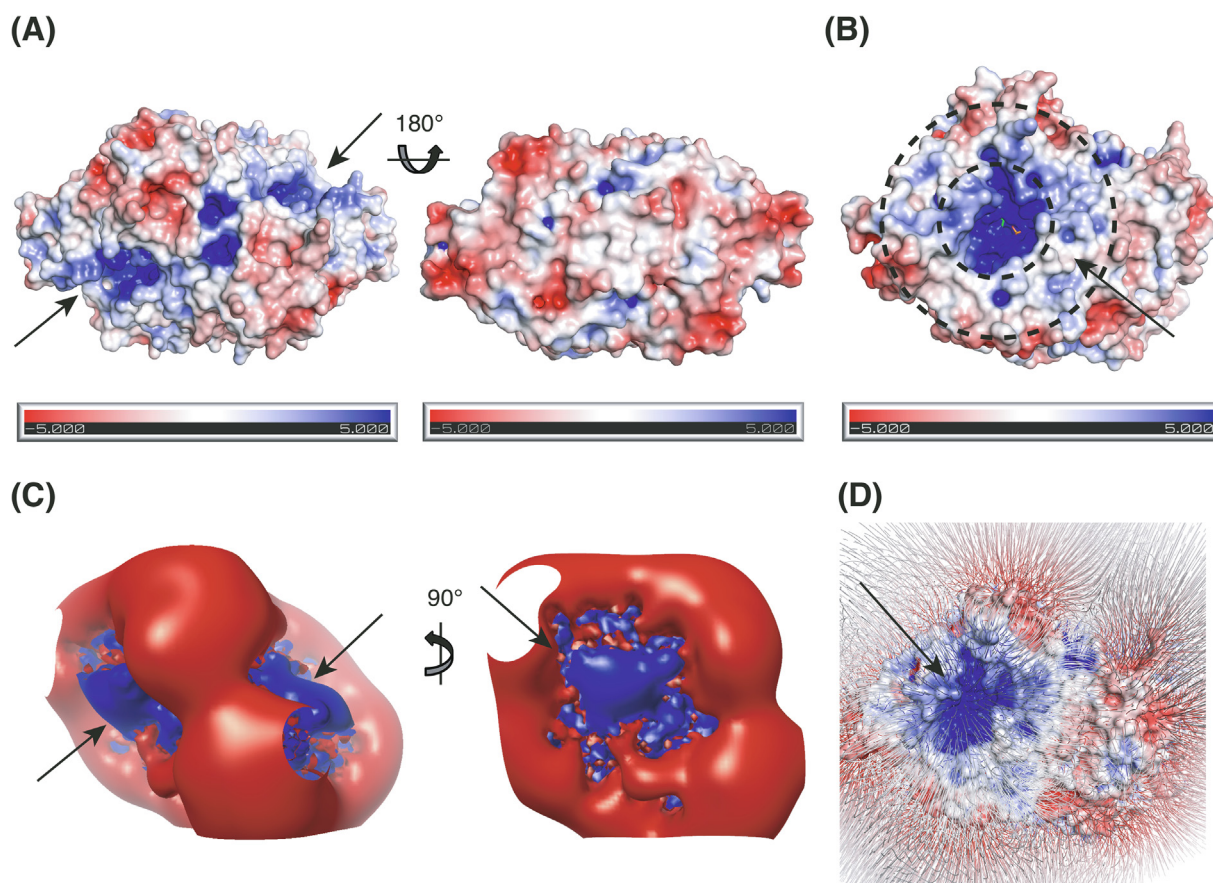
Fig. 3. Surface electrostatic potential of St-ωTA. (A) The surface electrostatic distribution of the dimer is shown in two different orientations. The scale ranges from −5 kT/e (red) to 5 kT/e (blue). Arrows indicate the active sites. (B) An aerial view of the active site of subunit A. The arrow indicates the hydrophobic region between the two dashed circles. (C) Electrostatic potential isocontours are shown as red (−1 kT/e) and blue (+1 kT/e) surfaces in two different orientations: a view representing the two active sites (left) and an aerial view of the active site of subunit A (right). Arrows indicate active sites. (D) Electric field generated by the surface electrostatic potential of St-ωTA. The surface electrostatic potential distribution is the same as in panels A and B. The electric field map is contoured at the −0.5 sigma level.

analyses revealed a notable feature of the cavity of St-ωTA compared with those of Vp-βTA and Ms-βTA. We found that the cavity of St-ωTA is larger than those of the others (Fig. 4C-E). The cavity volume of St-ωTA is 1217 Å³, whereas those of Vp-βTA and Ms-βTA are 781 Å³ and 1182 Å³, respectively. This means that St-ωTA is able to accept bulkier compounds as substrates. It is also noteworthy that the bottom of the St-ωTA cavity is proximal to PLP with unrestricted space (Fig. 4C), while that of the Vp-βTA cavity is separate from PLP in the grid map (Fig. 4D) and Ms-βTA has a bottleneck at the corresponding site (Fig. 4E). This spatially tolerant trait of St-ωTA is assumed to facilitate substrate accessibility to PLP for transamination. By contrast, Vp-βTA and Ms-βTA seem to physically restrict substrate selectivity, owing to the relatively narrow paths at the bottom of their cavities.

Besides the structural differences in their active sites, we also found that a long loop (S157-S193) between β5 and α6, together with α6 display striking spatial variations among the five enzymes (we denominate this loop and α6 as the V region) (Fig. 5A). St-ωTA has 37 residues in the V region, whereas the two βTAs have 17 residues. The length of V region in St-ωTA exceeds that of 31 residues in the corresponding region of the four GSAMs (Ba-GSAM, Bs-GSAM, Te-GSAM, and Ap-GSAM). The V region of St-ωTA protrudes outwards owing to its steric bulkiness compared with those of Vp-βTA and Ms-βTA. In addition, the V region of St-ωTA incorporates a short helix (α6) not present in Vp-βTA and Ms-βTA. Given that the GSAMs also retain these secondary structures in the corresponding region, St-ωTA has more topological similarity to the GSAMs than to the βTAs, at least with regard to the V region.

As shown in Fig. 1D, we investigated the evolutionary conservation in 150 homologues of St-ωTA. The V region exhibited sequence variation except in an interior region that includes α6 (Fig. 5B). The fact that this region is evolutionarily variable implies that it may be related to biophysical or functional peculiarities of individual enzymes.

To assess biophysical properties, we analyzed the *B*-factor distribution of the V region of St-ωTA, which indicates vibrational motion of the atoms that make up the V region. This analysis showed that the V region in subunit A exhibits extremely high *B*-factor values (Fig. 5C), while the V region in subunit B showed relatively low *B*-factor values despite a component of the dimer having 2-fold symmetry (Fig. 5C), suggesting that subunit A and B may be surrounded by different environments in the crystals. Hence, the packing environment in the crystal was investigated by measuring interaction distances between each subunit and its neighboring molecule. It was observed that the V region in subunit A weakly interacts with its neighboring molecule, whereas that in subunit B strongly interacts with the adjacent molecule (Fig. S4). Therefore, we conclude that the discrepancy in *B*-factor distribution between subunit A and B is due to different internal packing environments in the crystal. In addition, we observed that the four GSAMs, together with St-ωTA generally showed a high *B*-factor distribution pattern regardless of thermostability, in which Ba-GSAM, Te-GSAM, and Ap-GSAM have disordered segments of their V regions (Fig. S5). It is reasonable to surmise that their high *B*-factor distributions are caused by their relatively long loops in the V region.
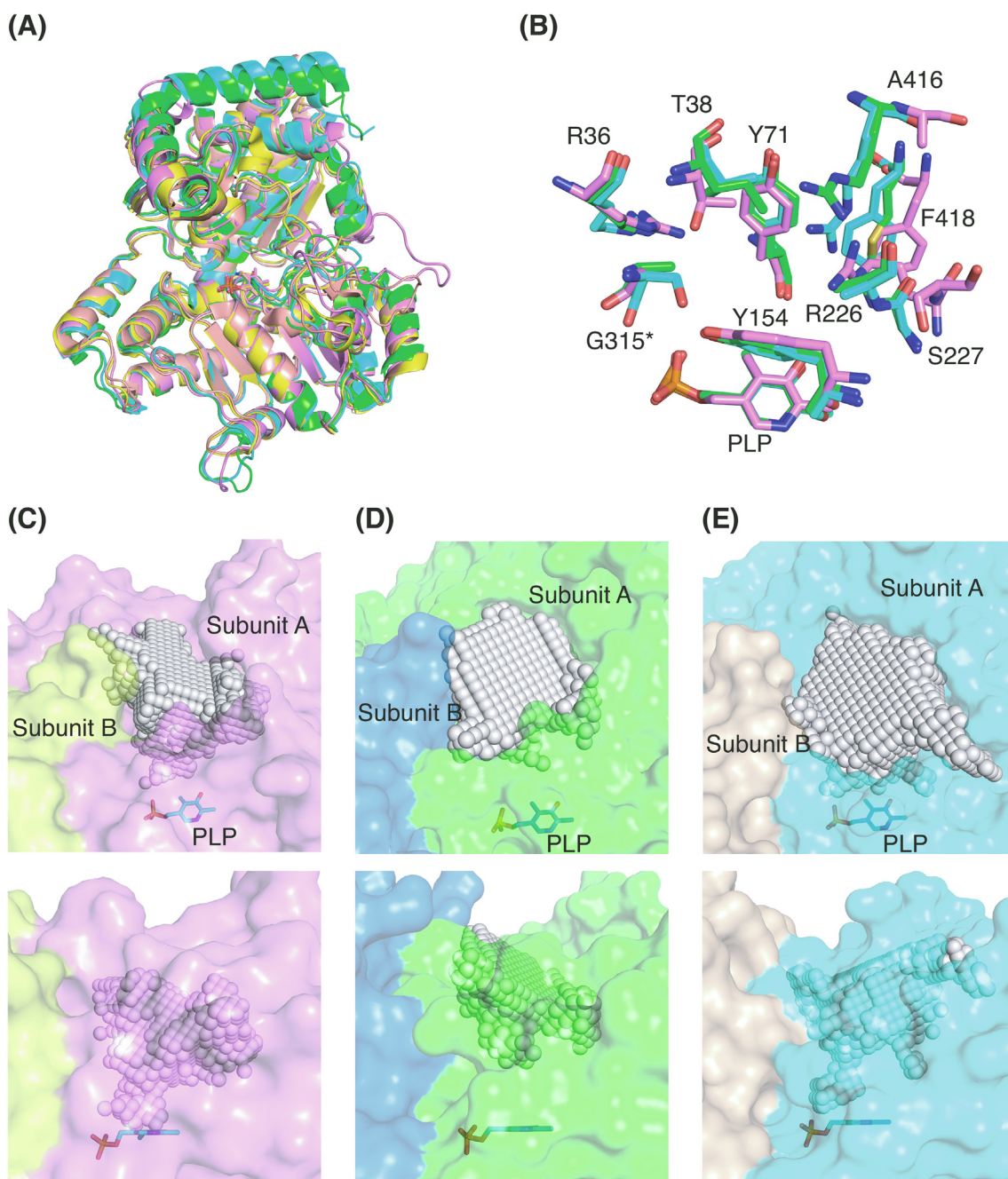
(A)

(B)

Fig. 4. Structural comparison of St-ωTA with homologues. (A) Overall structural comparison between St-ωTA and homologues. Subunit A of St-ωTA (violet) is superimposed onto the structures of homologues such as Vp-βTA (cyan), Ms-βTA (green), Ba-GSAM (yellow), and Bs-GSAM (salmon). The PLP cofactors are shown in stick representation. (B) Zoomed-in view of the active site residues and PLP. Those of St-ωTA, Vp-βTA, and Ms-βTA are colored violet, cyan, and green, respectively. The asterisk by G315 denotes that it originates from the other subunit. Steric analyses of the active site cavities of St-ωTA (C), Vp-βTA (D), and Ms-βTA (E). The lower panels show the lateral views of the upper panels, which are parallel to the PLP rings. The respective active site cavities are filled with virtual spheres.

3.5. Molecular docking simulations for substrate candidates

The enzymatic activity of St-ωTA has been described in a previous study focused on its biochemical characterization (Mathew et al., 2016). The study showed that St-ωTA exhibited discriminative enzymatic activity for amino group donor compounds and acceptor compounds. However, the molecular mechanism by which St-ωTA discriminates among specific compounds remains elusive. To address this issue, molecular docking simulations of candidate substrates were performed. Compounds with high and low activity from the biochemical study were selected as candidates for docking simulations. All candidate structures were generated as (S)-enantiomers, taking into

account that St-ωTA is (S)-enantioselective (Mathew et al., 2016). To investigate the spatial rearrangement of key residues in the active site, Arg36, Thr38, Tyr71, Tyr154, Arg226, Ser227, Ile258, and Phe418 were designated as flexible residues. For amino group acceptor docking, the PLP cofactor was replaced with PMP to provide a chemically reasonable environment.

Docking simulation results are summarized in Table S1 with ranks and binding energy values. Top-ranked conformers were selected for structural analysis. These docking simulations revealed that the five compounds with high relative activity in the previous study (Mathew et al., 2016) have a marked similarity in functional group orientation (Fig. S6A-E). Except in the case of compound D3, the carboxylic acid
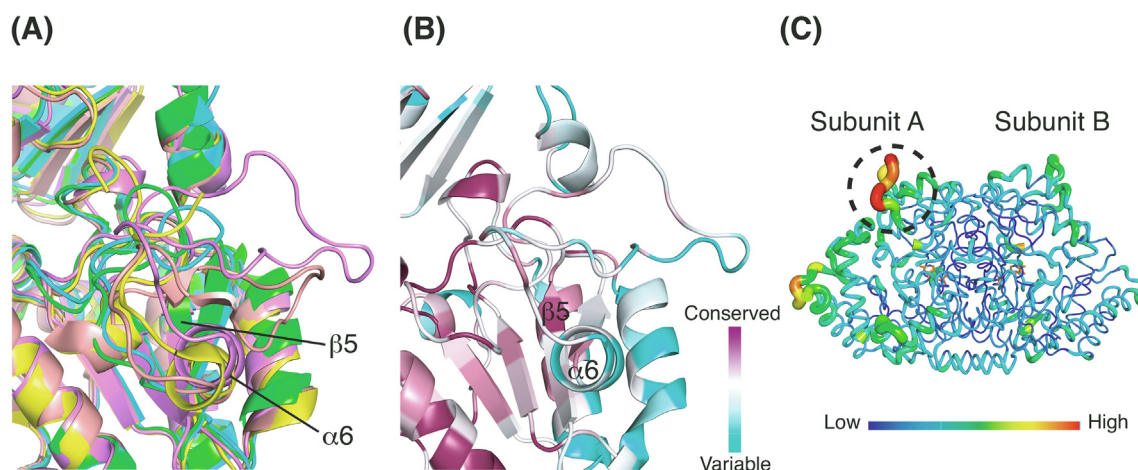
Fig. 5. Structural diversity of the V region. (A) Zoomed-in view of the V region. Structural comparison and color code are the same as in Fig. 4 (panel A). (B) Sequence variation within the V region. Color code is the same as in Fig. 1 (panel D). (C) *B*-factor distribution of St-ωTA. The dimeric structure is shown in putty representation. The dashed circle indicates the V region of subunit A.

group and hydrophobic group were spatially assigned to the P-pocket and O-pocket, respectively. An oxygen atom of the carboxylic acid group forms a salt bridge with Arg36, while the bulky hydrophobic group interacts with hydrophobic residues in the O-pocket. In particular, the aromatic ring in the hydrophobic group interacts with Tyr71 or Tyr154 by π-π stacking (Fig. S6B-E). It is noteworthy that the fluorine (compound D2) and oxygen atoms (compound D3 and D4) in the hydrophobic group form a salt bridge with Arg226 (Fig. S6B-D). Such electrostatic interactions are expected to contribute to stabilizing the hydrophobic group of the substrate upon binding to the O-pocket. These docking results elucidate why amino group donors retaining both a carboxylic acid group and an appropriate hydrophobic group exhibit high relative activity.

By contrast, compounds D6, D7, and D8 adopted unfavorable orientations of their functional groups, including the amino group (Fig. S6F-H). The methyl or ethyl groups of these candidates were assigned to the P-pocket, and the amino groups were not facing the C4′ atom of the PLP ring. In particular, compound D6 exhibited a remarkably high binding energy value probably owing to its extremely short functional groups (Table S1). Although the conformers of compounds D7 and D8 were energetically stable, inappropriate orientation of their amino group is assumed to have resulted in low enzymatic activity (Fig. S6G, H). We conclude that suitable interactions with both P- and O-pockets, together with appropriate orientation of the amino group constitute key factors for high enzymatic activity towards preferred substrates.

In addition to amino group donor compounds, amino group acceptor compounds were also subjected to docking simulations. The previous enzymatic study reported that pyruvate (compound A1), ethyl pyruvate (compound A2), and 2-oxohexanoate (compound A3) resulted in high enzymatic activity of St-ωTA (Mathew et al., 2016). Our docking simulation analysis showed that the carboxylic acid of compound A1 interacts with the hydroxide group of Thr38 (Fig. S6I), and the two oxygen atoms of compound A2 form salt bridges with Arg36 and Thr38 (Fig. S6J). In the case of compound A3, the carboxylic acid group forms hydrogen bonds with Thr38 and Tyr154 (Fig. S6K). The hydrophobic groups of these three conformers were oriented toward the O-pocket. However, compound A4 appears to be unable to strongly bind to the P- and O-pockets because of its short carbon chain and the absence of a hydrophilic functional group (Fig. S6L). Meanwhile, the fluorine atom of compound A5 was positioned in proximity to the ammonium group of PMP, suggesting that the fluorine atom may competitively interact with the ammonium group by forming a hydrogen bond (Fig. S6M). This interaction may hamper interaction of the ketone group of compound A5 with the amino group of PMP, thereby resulting in low enzymatic activity. Lastly, the ketone group of

compound A6 was oriented in the opposite direction from the nitrogen atom of PMP (Fig. S6N). Accordingly, although the binding energy value is relatively low, this unsuitable orientation may have resulted in enzymatic inactivity.

4. Discussion

The structure of St-ωTA corresponds to fold type I, in which a small domain is divided into two pieces by a large domain. On the other hand, TAs belonging to fold type IV, such as branched-chain amino acid aminotransferases, comprise two continuous domains, which are linked by an interdomain loop. In the St-ωTA structure, as shown in Fig. 1E, the large domain spatially divides the small domain into two lobes. It is plausible to postulate that an ancestral gene encoding the large domain was inserted into the middle of another ancestral gene encoding the small domain. The monomeric structure of St-ωTA clearly shows that the large domain is connected by long loops to the two lobes of the small domain (Fig. 1E). This loop-coding region in the ancestral small domain gene might have been vulnerable to heterogeneous gene insertion *ab extra*, taking into account that long loops tend to exhibit high evolutionary variability because they generally do not adopt a specific secondary structure. If our hypothesis is correct, fold type I TAs including St-ωTA constitute an example of evolutionary diversification strategy involving gene insertion and multimerization.

Previous studies of TA structures have revealed that the O- and P-pockets show variability in size and residue assignment (Humble et al., 2012; Wybenga et al., 2012; Midelfort et al., 2013). The St-ωTA structure also exhibited peculiar spatial arrangements of its active site residues. Most interestingly, compared with Vp-βTA and Ms-βTA, St-ωTA shows spatial inversion of Arg226 and Ala416 in its active site, thereby expanding the volume of the O-pocket. This subtle difference in positioning probably contributes to the broadening of the substrate specificity of St-ωTA. Our molecular docking results showed that Arg226 adopts diverse conformers in response to a variety of substrates. The flexibility of Arg226 appears to facilitate formation of hydrogen bonds to hydrophilic groups of the substrates, simultaneously adjusting the O-pocket space to optimize substrate binding. Considering that hydrophobic residues including Ala416 are involved in formation of the O-pocket, the position of Arg226 seemingly reduces the homogeneity of the O-pocket in terms of its hydrophobic property. However, the formation of hydrogen bonds by Arg226 could result in a more thermodynamically favorable environment. As seen in Fig. S6A-E, compounds containing hydrophilic groups can form hydrogen bonds to Arg226, thereby decreasing enthalpy despite binding to the hydrophobic O-pocket. As a consequence, such a unique assignment of Arg226 in the

active site is assumed to be a molecular strategy to minimize energy loss within the energetically unfavorable environment of the hydrophobic O-pocket when binding substrates containing a hydrophilic group.

We found that many water molecules are present in the active site cavity of St-ωTA. The presence of water molecules in the active site has been identified in TA structures revealed by X-ray crystallography thus far (Humble et al., 2012; Wybenga et al., 2012; Crismaru et al., 2013; Midelfort et al., 2013). We focus particularly on the specific water molecules involved in PLP fixation. Thirteen water molecules are directly or indirectly associated with formation of hydrogen bonds to PLP (Fig. 2E). These water molecules form a vast network of 28 hydrogen bonds. This number is higher than those in the active sites of Vp-βTA (17; 8 water molecules) and Ms-βTA (7; 3 water molecules). Given that thermostable St-ωTA has more water molecules in the proximity of PLP, and more hydrogen bonds compared with the thermolabile Vp-βTA and Ms-βTA, it is hypothesized that the water molecules involved in PLP fixation may play a vital role in maintaining the position of PLP, which allows St-ωTA to retain PLP in its active site in harsh conditions such as high temperature.

Indeed, some reports have demonstrated that retention of PLP or PMP in the active site is critical to stability and subunit assembly (Mishra et al., 2011; Börner et al., 2017). A biophysical study showed that the PLP-incorporated holo form is more stable than the apo form of a phosphoserine aminotransferase from *Entamoeba histolytica*, exhibiting a higher melting temperature and denaturant concentration (Mishra et al., 2011). Börner et al. also reported that dissociation of PMP from the holo forms of TAs induces aggregation of the apo enzymes (Börner et al., 2017). As of now, it is not clear to what extent water molecules forming a hydrogen bond network for PLP fixation affect PLP retention and stability of the holo form because there are other stabilization factors such as charge-charge and hydrophobic interactions between PLP and adjacent residues. Nevertheless, it seems possible that the water molecules exert a buffering effect to maintain stability at high temperatures.

A striking surface feature of St-ωTA is that positively charged residues predominate within the active site cavity, whereas regions surrounding the active site entrance have negatively charged residues (Fig. 3B). This seems to be a common biophysical property observed among TAs (Kwon et al., 2019; Kwon and Park, 2019b). The electric field generated by such charge distributions is predicted to constitute a strong driving force to attract PLP and amino group acceptors into the active site. Considering that PLP and amino group acceptor molecules have relatively strong negative charges, the electrostatic steering to attract them into the active site regardless of specificity could be a probabilistic tactic to obtain two of the three kinds of binding molecules required for activity (PLP, an amino group donor, and an amino group acceptor). This suggests the possibility that amino group donors play a role as the target that generates specificity. This scenario is plausible, because amino group donors generally have a net charge of 0 and are more strongly associated with substrate specificity than amino group acceptors.

It is unclear what happens structurally after substrate transfer to the active site, although it is noteworthy that the loop in the V region of St-ωTA shows high mobility. This loop corresponds to the "gating loop" located near the active site of GSAMs. For GSAMs, the loop has been known to play a role as a lid to cover the active site after substrate binding (Stetefeld et al., 2006; Campanini et al., 2013). For example, a structural study on a GSAM from *Synechococcus* (S-GSAM) revealed that the gating loop exhibits a remarkable conformational change between open and closed forms of the enzyme, depending on the chemical state of PLP (Stetefeld et al., 2006). This study also reported that both forms of the loop were concurrently observed in a dimer, suggesting that the two subunits communicate with each other for catalysis (Stetefeld et al., 2006). Unlike Vp-βTA and Ms-βTA, St-ωTA has a loop similar to that of S-GSAM. Accordingly, the loop observed in St-ωTA may function as a gating loop regulating access to the active site. Considering that a

number of water molecules can enter the active site owing to the voluminous active site cavity of St-ωTA, it seems to be necessary to block entry of bulk water to the active site entrance to favor catalytic reactions.

5. Conclusions

We herein describe the structure of thermostable St-ωTA containing PLP as a cofactor. A prior biochemical study documented that St-ωTA possesses enzymatic activity toward a wide range of substrates, such as amines and β- and γ-amino acids, and exhibits remarkable thermostability (Mathew et al., 2016). The St-ωTA structure revealed the specific active site pocket formed by a unique arrangement of conserved residues. The unique arrangement is probably related to its enzymatic specificity. It is also implied that a set of water molecules in the active site may affect the thermal stability of St-ωTA. In addition, molecular docking simulations showed how the P- and O-pockets at the active site can bind to the functional groups of substrate compounds for catalysis, and how the orientation and assignment of the functional groups can contribute to enzymatic activity. Our crystal structure, together with the electrostatic steering model, provides structural bases for comprehensive elaboration of the enzymatic mechanism of St-ωTA. The present study thus expands our structural and functional understanding of St-ωTA. Some questions remain to be answered: 1) Do the actual rearrangements of active site residues upon substrate binding agree with our docking simulation results? 2) Does the loop in the V region undergo a drastic conformational change to cover the active site after substrate entry as we expect? 3) Is St-ωTA also able to catalyze isomerization of glutamate-1-semialdehyde to 5-aminolevulinate as GSAMs? Notwithstanding these issues to be addressed in future studies, our results establish a structural basis for a profound understanding of St-ωTA.

Data availability

The atomic coordinates and structure factors for St-ωTA have been deposited in the Protein Data Bank (http://www.rcbs.org) under accession code 6K8H.

Declaration of Competing Interest

The authors declare that they have no known competing financial interests or personal relationships that could have appeared to influence the work reported in this paper.

Acknowledgements

Appendix A. Supplementary data

Supplementary data to this article can be found online at https://doi.org/10.1016/j.jsb.2019.09.012.

References

Adams, P.D., Afonine, P.V., Bunkóczi, G., Chen, V.B., Davis, I.W., Echols, N., Headd, J.J., Hung, L.W., Kapral, G.J., Grosse-Kunstleve, R.W., McCoy, A.J., Moriarty, N.W., Oeffner, R., Read, R.J., Richardson, D.C., Richardson, J.S., Terwilliger, T.C., Zwart, P.H., 2010. PHENIX: a comprehensive Python-based system for macromolecular structure solution. Acta Crystallogr. D Biol. Crystallogr. 66, 213–221.

Afonine, P.V., Grosse-Kunstleve, R.W., Echols, N., Headd, J.J., Moriarty, N.W., Mustyakimov, M., Terwilliger, T.C., Urzhumtsev, A., Zwart, P.H., Adams, P.D., 2012. Towards automated crystallographic structure refinement with phenix.refine. Acta

Crystallogr. D Biol. Crystallogr. 68, 352–367.

Ashkenazy, H., Erez, E., Martz, E., Pupko, T., Ben-Tal, N., 2010. ConSurf 2010: calculating evolutionary conservation in sequence and structure of proteins and nucleic acids. Nucl. Acids Res. 38, W529–W533.

Bezsudnova, E.Y., Boyko, K.M., Popov, V.O., 2017. Properties of bacterial and archaeal branched-chain amino acid aminotransferases. Biochemistry (Moscow) 82, 1572–1591.

Boyko, K.M., Stekhanova, T.N., Nikolaeva, A.Y., Mardanov, A.V., Rakitin, A.L., Ravin, N.V., Bezsudnova, E.Y., Popov, V.O., 2016. First structure of archaeal branched-chain amino acid aminotransferase from *Thermoproteus uzoniensis* specific for L-amino acids and R-amines. Extremophiles 20, 215–225.

Börner, T., Rämisch, S., Reddem, E.R., Bartsch, S., Vogel, A., Thunnissen, A.W.H., Adlercreutz, P., Grey, C., 2017. Explaining operational instability of amine transaminases: substrate-induced inactivation mechanism and influence of quaternary structure on enzyme-cofactor intermediate stability. ACS Catal. 7, 1259–1269.

Campanini, B., Bettati, S., Di Salvo, M.L., Mozzarelli, A., Contestabile, R., 2013. Asymmetry of the active site loop conformation between subunits of glutamate-1-semialdehyde aminomutase in solution. Biomed. Res. Int. 2013, 353270.

Cooper, A.J., Meister, A., 1989. An appreciation of Professor Alexander E. Braunstein. The discovery and scope of enzymatic transamination. Biochimie 71, 387–404.

Crismaru, C.G., Wybenga, G.G., Szymanski, W., Wijma, H.J., Wu, B., Bartsch, S., de Wildeman, S., Poelarends, G.J., Feringa, B.L., Dijkstra, B.W., Janssen, D.B., 2013. Biochemical properties and crystal structure of a β-phenylalanine aminotransferase from *Variovorax paradoxus*. Appl. Environ. Microbiol. 79, 185–195.

Emsley, P., Cowtan, K., 2004. Coot: model-building tools for molecular graphics. Acta Crystallogr. D Biol. Crystallogr. 60, 2126–2132.

Fuchs, M., Farnberger, J.E., Kroutil, W., 2015. The industrial age of biocatalytic transamination. Eur. J. Org. Chem. 32, 6965–6982.

Ge, H., Lv, X., Fan, J., Gao, Y., Teng, M., Niu, L., 2010. Crystal structure of glutamate-1-semialdehyde aminotransferase from Bacillus subtilis with bound pyridoxamine-5'-phosphate. Biochem. Biophys. Res. Commun. 402, 356–360.

Guo, F., Berglund, P., 2017. Transaminase biocatalysis: optimization and application. Green Chem. 19, 333–360.

Hanwell, M.D., Curtis, D.E., Lonie, D.C., Vandermeersch, T., Zurek, E., Hutchison, G.R., 2012. Avogadro: an advanced semantic chemical editor, visualization, and analysis platform. J. Cheminform 4, 17.

Hayashi, H., 1995. Pyridoxal enzymes: mechanistic diversity and uniformity. J. Biochem. 118, 463–473.

Hirotsu, K., Goto, M., Okamoto, A., Miyahara, I., 2005. Dual substrate recognition of aminotransferases. Chem. Rec. 5, 160–172.

Holm, L., Laakso, L.M., 2016. Dali server update. Nucl. Acids Res. 44, W351–W355.

Humble, M.S., Cassimjee, K.E., Håkansson, M., Kimbung, Y.R., Walse, B., Abedi, V., Federsel, H.J., Berglund, P., Logan, D.T., 2012. Crystal structures of the *Chromobacterium violaceum* ω-transaminase reveal major structural rearrangement upon binding of coenzyme PLP. FEBS J. 279, 779–792.

Jurrus, E., Engel, D., Star, K., Monson, K., Brandi, J., Felberg, L.E., Brookes, D.H., Wilson, L., Chen, J., Liles, K., Chun, M., Li, P., Gohara, D.W., Dolinsky, T., Konecny, R., Koes, D.R., Nielsen, J.E., Head-Gordon, T., Geng, W., Krasny, R., Wei, G.W., Holst, M.J., McCammon, J.A., Baker, N.A., 2018. Improvements to the APBS biomolecular solvation software suite. Protein Sci. 27, 112–128.

Koszelewski, D., Göritzer, M., Clay, D., Seisser, B., Kroutil, W., 2010a. Synthesis of optically active amines employing recombinant ω-transaminases in *E. coli* cells. ChemCatChem 2, 73–77.

Koszelewski, D., Tauber, K., Faber, K., Kroutil, W., 2010b. ω-transaminases for the synthesis of non-racemic α-chiral primary amines. Trends Biotechnol. 28, 324–332.

Krissinel, E., Henrick, K., 2007. Inference of macromolecular assemblies from crystalline state. J. Mol. Biol. 372, 774–797.

Kwon, S., Lee, J.H., Kim, C.M., Jang, H., Yun, H., Jeon, J.H., So, I., Park, H.H., 2019. Structural basis of substrate recognition by a novel thermostable (*S*)-enantioselective ω-transaminase from *Thermomicrobium roseum*. Sci. Rep. 9, 6958.

Kwon, S., Park, H.H., 2019a. Structural consideration of the working mechanism of fold type I transaminases from eubacteria: overt and covert movement. Comput. Struct. Biotechnol. J. 17, 1031–1039.

Kwon, S., Park, H.H., 2019b. Crystal structure of the apo form of a β-transaminase from *Mesorhizobium* sp. strain LUK. Protein Sci. 28, 964–970.

Langer, G., Cohen, S.X., Lamzin, V.S., Perrakis, A., 2008. Automated macromolecular model building for X-ray crystallography using ARP/wARP version 7. Nat. Protoc. 3,

1171–1179.

Laskowski, R.A., MacArthur, M.W., Moss, D.S., Thornton, J.M., 1993. PROCHECK: a program to check the stereochemical quality of protein structures. J. Appl. Cryst. 26, 283–291.

Laskowski, R.A., Swindells, M.B., 2011. LigPlot+: multiple ligand-protein interaction diagrams for drug discovery. J. Chem. Inf. Model. 24, 2778–2786.

Malik, M.S., Park, E.S., Shin, J.S., 2012. Features and technical applications of ω-transaminases. Appl. Microbiol. Biotechnol. 94, 1163–1171.

Mathew, S., Nadarajan, S.P., Chung, T., Park, H.H., Yun, H., 2016. Biochemical characterization of thermostable ω-transaminase from Sphaerobacter thermophilus and its application for producing aromatic β- and γ-amino acids. Enzyme Microb. Technol. 87–88, 52–60.

McCoy, A.J., Grosse-Kunstleve, R.W., Adams, P.D., Winn, M.D., Storoni, L.C., Read, R.J., 2007. Phaser crystallographic software. J. Appl. Crystallogr. 40, 658–674.

Midelfort, K.S., Kumar, R., Han, S., Karmilowicz, M.J., McConnell, K., Gehlhaar, D.K., Mistry, A., Chang, J.S., Anderson, M., Villalobos, A., Minshull, J., Govindarajan, S., Wong, J.W., 2013. Redesigning and characterizing the substrate specificity and activity of *Vibrio fluvialis* aminotransferase for the synthesis of imagabalin. Protein Eng. Des. Sel. 26, 25–33.

Mishra, V., Ali, V., Nozaki, T., Bhakuni, V., 2011. Biophysical characterization of *Entamoeba histolytica* phosphoserine aminotransferase (EhPSAT): role of cofactor and domains in stability and subunit assembly. Eur. Biophys. J. 40, 599–610.

Morris, G.M., Huey, R., Lindstrom, W., Sanner, M.F., Belew, R.K., Goodsell, D.S., Olson, A.J., 2009. AutoDock4 and AutoDockTools4: automated docking with selective receptor flexibility. J. Comput. Chem. 30, 2785–2791.

Murshudov, G.N., Skubák, P., Lebedev, A.A., Pannu, N.S., Steiner, R.A., Nicholls, R.A., Winn, M.D., Long, F., Vagin, A.A., 2011. REFMAC5 for the refinement of macromolecular crystal structures. Acta Crystallogr. D Biol. Crystallogr. 67, 355–367.

Oosterwijk, N.V., Willies, S., Hekelaar, J., Terwisscha van Scheltinga, A.C., Turner, N.J., Dijkstra, B.W., 2016. Structural basis of the substrate range and enantioselectivity of two (S)-selective ω-transaminases. Biochemistry 55, 4422–4431.

Otwinowski, Z., Minor, W., 1997. Processing of X-ray diffraction data collected in oscillation mode. Methods Enzymol. 276, 307–326.

Park, E.S., Kim, M., Shin, J.S., 2012. Molecular determinants for substrate selectivity of ω-transaminases. Appl. Microbiol. Biotechnol. 93, 2425–2435.

Robert, X., Gouet, P., 2014. Deciphering key features in protein structures with the new ENDscript server. Nucl. Acids Res. 42, 320–324.

Schiroli, D., Peracchi, A., 2015. A subfamily of PLP-dependent enzymes specialized in handling terminal amines. Biochim. Biophys. Acta 1854, 1200–1211.

Schrödinger, L., 2006. The PyMOL Molecular Graphics System, Version 1.7.4. Schrödinger LLC.

Schulze, J.O., Schubert, W.D., Moser, J., Jahn, D., Heinz, D.W., 2006. Evolutionary relationship between initial enzymes of tetrapyrrole biosynthesis. J. Mol. Biol. 358, 1212–1220.

Sievers, F., Wilm, A., Dineen, D., Gibson, T.J., Karplus, K., Li, W., Lopez, R., McWilliam, H., Remmert, M., Soding, J., Thompson, J.D., Higgins, D.G., 2011. Fast, scalable generation of high-quality protein multiple sequence alignments using Clustal Omega. Mol. Syst. Biol. 7, 539.

Slabu, I., Galman, J.L., Lloyd, R.C., Turner, N.J., 2017. Discovery, engineering, and synthetic application of transaminase biocatalysts. ACS Catal. 7, 8263–8284.

Stefefeld, J., Jenny, M., Burkhard, P., 2006. Intersubunit signaling in glutamate-1-semialdehyde-aminomutase. Proc. Natl. Acad. Sci. U.S.A. 103, 13688–13693.

Toney, M.D., 2011. Controlling reaction specificity in pyridoxal phosphate enzymes. Biochim. Biophys. Acta 1814, 1407–1418.

Trott, O., Olson, A.J., 2010. AutoDock Vina: improving the speed and accuracy of docking with a new scoring function, efficient optimization and multithreading. J. Comput. Chem. 31, 455–461.

Yu, J., Zhou, Y., Tanaka, I., Yao, M., 2010. Roll: a new algorithm for the detection of protein pockets and cavities with a rolling probe sphere. Bioinformatics 26, 46–52.

Winn, M.D., Ballard, C.C., Cowtan, K.D., Dodson, E.J., Emsley, P., Evans, P.R., Keegan, R.M., Krissinel, E.B., Leslie, A.G., McCoy, A., McNicholas, S.J., Murshudov, G.N., Pannu, N.S., Potterton, E.A., Read, R.J., Vagin, A., Wilson, K.S., 2011. Overview of the CCP4 suite and current developments. Acta Crystallogr. D Biol. Crystallogr. 67, 235–242.

Wybenga, G.G., Crismaru, C.G., Janssen, D.B., Dijkstra, B.W., 2012. Structural determinants of the β-selectivity of a bacterial aminotransferase. J. Biol. Chem. 287, 28495–28502.